Biomedical Optics EXPRESS

Histology validation of mapping depth-resolved cardiac fiber orientation in fresh mouse heart using optical polarization tractography

Y. Wang,[1] K. Zhang,[2] N. B. Wasala,[2] X. Yao,[1] D. Duan,[2] and G. Yao[1,*]

[1]*Department of Bioengineering, University of Missouri, Columbia, MO 65211, USA*
[2]*Department of Molecular Microbiology & Immunology, University of Missouri, Columbia, MO 65211, USA*
**yaog@missouri.edu*

Abstract: Myofiber organization in cardiac muscle plays an important role in achieving normal mechanical and electrical heart functions. An imaging tool that can reveal microstructural details of myofiber organization is valuable for both basic research and clinical applications. A high-resolution optical polarization tractography (OPT) was recently developed based on Jones matrix optical coherence tomography (JMOCT). In this study, we validated the accuracy of using OPT for measuring depth-resolved fiber orientation in fresh heart samples by comparing directly with histology images. Systematic image processing algorithms were developed to register OPT with histology images. The pixel-wise differences between the two tractographic results were analyzed in details. The results indicate that OPT can accurately image depth-resolved fiber orientation in fresh heart tissues and reveal microstructural details at the histological level.

©2014 Optical Society of America

OCIS codes: (110.4500) Optical coherence tomography; (230.5440) Polarization-selective devices; (170.6935) Tissue characterization.

References and links

1. B. Taccardi, E. Macchi, R. L. Lux, P. R. Ershler, S. Spaggiari, S. Baruffi, and Y. Vyhmeister, "Effect of myocardial fiber direction on epicardial potentials," Circulation **90**(6), 3076–3090 (1994).
2. D. D. Streeter, Jr., H. M. Spotnitz, D. P. Patel, J. Ross, Jr., and E. H. Sonnenblick, "Fiber orientation in the canine left ventricle during diastole and systole," Circ. Res. **24**(3), 339–347 (1969).
3. A. G. Kléber and Y. Rudy, "Basic Mechanisms of Cardiac Impulse Propagation and Associated arrhythmias," Physiol. Rev. **84**(2), 431–488 (2004).
4. G. J. Strijkers, A. Bouts, W. M. Blankesteijn, T. H. Peeters, A. Vilanova, M. C. van Prooijen, H. M. Sanders, E. Heijman, and K. Nicolay, "Diffusion tensor imaging of left ventricular remodeling in response to myocardial infarction in the mouse," NMR Biomed. **22**(2), 182–190 (2009).
5. D. E. Sosnovik, R. Wang, G. Dai, T. G. Reese, and V. J. Wedeen, "Diffusion MR tractography of the heart," J. Cardiovasc. Magn. Reson. **11**(1), 47 (2009).
6. C. M. Ambrosi, V. V. Fedorov, R. B. Schuessler, A. M. Rollins, and I. R. Efimov, "Quantification of fiber orientation in the canine atrial pacemaker complex using optical coherence tomography," J. Biomed. Opt. **17**(7), 071309 (2012).
7. C. P. Fleming, C. M. Ripplinger, B. Webb, I. R. Efimov, and A. M. Rollins, "Quantification of cardiac fiber orientation using optical coherence tomography," J. Biomed. Opt. **13**(3), 030505 (2008).
8. C. J. Goergen, H. Radhakrishnan, S. Sakadžić, E. T. Mandeville, E. H. Lo, D. E. Sosnovik, and V. J. Srinivasan, "Optical coherence tractography using intrinsic contrast," Opt. Lett. **37**(18), 3882–3884 (2012).
9. Y. Gan and C. P. Fleming, "Extracting three-dimensional orientation and tractography of myofibers using optical coherence tomography," Biomed. Opt. Express **4**(10), 2150–2165 (2013).
10. B. H. Park, M. C. Pierce, B. Cense, and J. F. de Boer, "Jones matrix analysis for a polarization-sensitive optical coherence tomography system using fiber-optic components," Opt. Lett. **29**(21), 2512–2514 (2004).
11. S. Makita, M. Yamanari, and Y. Yasuno, "Generalized Jones matrix optical coherence tomography: performance and local birefringence imaging," Opt. Express **18**(2), 854–876 (2010).
12. C. Fan and G. Yao, "Single camera spectral domain polarization-sensitive optical coherence tomography using offset B-scan modulation," Opt. Express **18**(7), 7281–7287 (2010).
13. C. Fan and G. Yao, "Full-range spectral domain Jones matrix optical coherence tomography using a single spectral camera," Opt. Express **20**(20), 22360–22371 (2012).

#213714 - $15.00 USD Received 9 Jun 2014; revised 24 Jul 2014; accepted 24 Jul 2014; published 29 Jul 2014

14. C. Fan and G. Yao, "Correcting optical-axis calculation in polarization-sensitive optical coherence tomography," IEEE Trans. Biomed. Eng. **57**(10), 2556–2559 (2010).
15. M. Todorović, S. Jiao, L. V. Wang, and G. Stoica, "Determination of local polarization properties of biological samples in the presence of diattenuation by use of Mueller optical coherence tomography," Opt. Lett. **29**(20), 2402–2404 (2004).
16. S. Jiao, M. Todorović, G. Stoica, and L. V. Wang, "Fiber-based polarization-sensitive Mueller matrix optical coherence tomography with continuous source polarization modulation," Appl. Opt. **44**(26), 5463–5467 (2005).
17. C. Fan and G. Yao, "Mapping local retardance in birefringent samples using polarization sensitive optical coherence tomography," Opt. Lett. **37**(9), 1415–1417 (2012).
18. C. Fan and G. Yao, "Mapping local optical axis in birefringent samples using polarization-sensitive optical coherence tomography," J. Biomed. Opt. **17**(11), 110501 (2012).
19. C. Fan and G. Yao, "Imaging myocardial fiber orientation using polarization sensitive optical coherence tomography," Biomed. Opt. Express **4**(3), 460–465 (2013).
20. Y. Wang and G. Yao, "Optical tractography of the mouse heart using polarization-sensitive optical coherence tomography," Biomed. Opt. Express **4**(11), 2540–2545 (2013).
21. A. E. H. Emery and F. Muntoni, *Duchenne Muscular Dystrophy* (Oxford University Press 2003).
22. W. J. Karlon, J. W. Covell, A. D. McCulloch, J. J. Hunter, and J. H. Omens, "Automated measurement of myofiber disarray in transgenic mice with ventricular expression of ras," Anat. Rec. **252**(4), 612–625 (1998).
23. S. Ortiz, D. Siedlecki, I. Grulkowski, L. Remon, D. Pascual, M. Wojtkowski, and S. Marcos, "Optical distortion correction in Optical Coherence Tomography for quantitative ocular anterior segment by three-dimensional imaging," Opt. Express **18**(3), 2782–2796 (2010).
24. M. Zhao, A. N. Kuo, and J. A. Izatt, "3D refraction correction and extraction of clinical parameters from spectral domain optical coherence tomography of the cornea," Opt. Express **18**(9), 8923–8936 (2010).
25. I. J. LeGrice, B. H. Smaill, L. Z. Chai, S. G. Edgar, J. B. Gavin, and P. J. Hunter, "Laminar structure of the heart: ventricular myocyte arrangement and connective tissue architecture in the dog," Am. J. Physiol.-Heart. C. **269**(2 38–2), H571–H582 (1995).
26. E. W. Hsu, A. L. Muzikant, S. A. Matulevicius, R. C. Penland, and C. S. Henriquez, "Magnetic resonance myocardial fiber-orientation mapping with direct histological correlation," Am. J. Physiol. **274**(5 Pt 2), H1627–H1634 (1998).
27. G. K. Rohde, A. Aldroubi, and B. M. Dawant, "The adaptive bases algorithm for intensity-based nonrigid image registration," IEEE Trans. Med. Imaging **22**(11), 1470–1479 (2003).

1. Introduction

Myofiber organization in cardiac muscle greatly influences the mechanical and electrical function of the heart [1, 2]. Action potential propagation is 2.1 to 10 times faster [3] along the longitudinal direction of cardiac myofibers than at the transverse direction. Myofiber disorganization compromises cardiac function. And alterations in cardiac muscle structure have been found as a result of cardiovascular disorders such as myocardial infarction [4]. Therefore "tractography", an imaging tool that can visualize microstructural details of myofiber organization, is valuable for both basic research and clinical applications. Despite its superior spatial resolution, histological assessment is time consuming and limited to imaging of small areas of fixed tissue. Alternatively, diffusion-tensor based magnetic resonance imaging (DTI) [5] has been established as a state-of-art method for imaging the 3D fiber organization in the heart; however, the image resolution in DTI is usually limited to submillimeters. Such a resolution is not sufficient for revealing microstructural details especially in mouse models which are widely used in cardiovascular research.

High resolution optical coherence tomography (OCT) has been explored to quantify fiber orientation in heart muscles [6–9]. This intensity-based method requires a high enough spatial resolution to resolve individual muscle fibers. The myocardial fibers in small animals such as mice typically have a diameter less than 3.0 μm. Although OCT systems with a ~1 μm spatial resolution is available, it is challenging to achieve simultaneously a large field of view and depth of view required for imaging in a large tissue e.g. the entire mouse heart.

We recently developed a high-resolution optical tractography method based on Jones matrix optical coherence tomography (JMOCT) [10–13]. Our technology can derive the depth-resolved local polarization properties including optical axis, retardation, and diattenuation from conventional cumulative results [13]. Because the local (slow) optical axis is aligned with fiber axis, it can be used to map fiber orientation within the imaging plane [14]. Measuring fiber orientation from local optical axis has been previously investigated

#213714 - $15.00 USD Received 9 Jun 2014; revised 24 Jul 2014; accepted 24 Jul 2014; published 29 Jul 2014
(C) 2014 OSA

using time-domain Mueller matrix PSOCT [15, 16]. However, these early studies only obtained fiber orientation at a few discrete depths along a single A-line even with a significant amount of averaging [15, 16]. Our Jones matrix based method [17, 18] greatly improved signal-to-noise and enabled tractography in 3D tissues [19, 20]. This new tractography technology inherits the intrinsic advantages of high resolution and fast imaging speed in OCT. It can measure fiber orientation with a single pixel resolution without the need of a super-high resolution OCT to resolve individual muscle fibers. For convenience, we refer to this technology for mapping depth-resolved fiber orientation as Optical Polarization Tractography (OPT).

We have demonstrated the capability of OPT in samples with homogeneous optical axis as well as in samples with depth-varying optical axis [18]. Most recently, we applied this technology for imaging fiber orientation in a bovine heart sample [19] and a fixed mouse heart [20]. Overall these studies showed good agreement with current knowledge of the myocardial fiber architecture in heart. In this study, we further validated the accuracy of OPT technology by comparing the optical tractography results directly with histology images obtained from the mouse heart. A comprehensive methodology was developed to correct the image distortions in OPT and register the optical tractography with histology images. The results showed that OPT technology can accurately image depth-resolved fiber organization in fresh heart tissues and can reveal microstructural details at the histological level.

2. Method

2.1 Tissue preparation and histology processing

A total of seven 2 to 6-m-old mice were used in this study including four C57BL/10 mice and three mdx mice [21]. The mouse heart was excised immediately after euthanasia. A small piece of the heart tissue of roughly 2~4 mm in size was cut from either the left or right ventricles from each heart. This piece of heart tissue was imaged first using the OPT system. Then the tissue sample was embedded in optimal cutting compound and frozen in liquid nitrogen. For histology processing, the tissue block was cut into 10 μm slices starting from the epicardium side. The histology slices were equivalent to the OCT *en face* imaging plane, i.e. the plane formed by the B- and C-scan directions at a specific depth from the epicardium. All tissue slices were numbered including damaged slices which, however, were not used in histology imaging. Tissue sections were stained with hematoxylin and eosin for microscopic imaging using a Nikon Eclipse E800 microscope equipped with a QImaging RETIGA 1300 camera.

2.2 Fiber orientation measurement using OPT

Our OPT method was implemented in a spectral domain full-range JMOCT system that has been described in detail previously [12, 13]. This bulk-optical system used a SLD source (SLD-351-HP, Superlum, Ireland) with a central wavelength of 847.8 nm. A telecentric scan lens (LSM03-BB, Thorlabs, Newton, NJ) was used as the imaging objective. Jones matrix measurement was achieved by using two alternating incident polarization states: left- and right-circular polarization. An electro-optical modulator (EO-AM-NR-C1, Thorlabs, Newton, NJ) was used to modulate the incident polarization. For each incident polarization, the two orthogonal polarization components (vertical- and horizontal-polarization) of the backscattered signal were detected in the spectral domain using a custom spectrometer [12, 13]. A 1024-pixel line scan CCD camera (AVIIVA SM2, e2v, Milpitas, CA) was used as the detector.

The JMOCT system was carefully calibrated following a procedure described in [13]. The lateral resolution of the system was measured as 11.4 μm and the depth resolution was measured as 8.1 μm in air (5.9 μm in tissue with a refractive index of 1.38). The JMOCT system had an imaging speed of 50,000 A-lines/sec. One 3D scan covered an imaging volume

#213714 - $15.00 USD Received 9 Jun 2014; revised 24 Jul 2014; accepted 24 Jul 2014; published 29 Jul 2014
(C) 2014 OSA

of 1.1 × 8.0 × 8.0 mm^3 with 280 × 2000 × 1000 pixels in A-B-C scan direction, leading to pixel sizes of 3.9 μm, 4.0 μm, and 8.0 μm in the A, B, and C-scan, respectively. In image processing, the 3D data set was resized using cubic spline to have the same pixel size of 3.9 μm in all three dimensions. The measured system sensitivity was 108 dB and 104 dB at 0.5 mm and 1.0 mm from the zero delay line, respectively.

A Jones calculus based algorithm was used to derive the depth-resolved local retardance (δ), diattenuation (σ), and optical axis orientation (θ) in addition to the intensity images (I). The retardance is defined as $2\pi d\Delta n/\lambda$ where Δn is the difference in refractive indices along the fast and slow optical axes and d is the physical pathlength (pixel size). The diattenuation is defined as the difference in optical attenuation coefficients along the fast and slow optical axes. The "local" retardance and diattenuation were effective results averaged over a single image pixel. The detailed procedure to derive local polarization properties was described elsewhere [19]. Briefly, each image pixel was modeled by a Jones matrix with an assigned set of polarization properties (δ, σ, θ). The local retardance and diattenuation were first calculated from the measured cumulative Jones matrices at adjacent axial pixels using similar matrix transformation [11, 19]. Then the local optical axis was calculated using an iterative algorithm starting from the sample surface [18, 19]. The previously obtained local retardance was used to construct the local Jones matrix; whereas the local diattenuation was eliminated from the process [19]. Fiber orientation was determined based on the angle of slow optical axis which ranged from −90° to 90° with the C-scan direction as the zero degree. To compare with histology results, the fiber orientation maps were constructed in the *en face* planes (B-C plane) at each depth with an axial pixel size of 3.9 μm/pixel [19, 20]. To improve signal-to-noise, the obtained fiber orientation image in the B-C plane was filtered using a 3 × 3 mean filter. The tractographic images were obtained by visualizing the optical axis images using the streamline or quiver functionalities in Matlab.

2.3 Fiber orientation measurement using histology image

Due to the labor intensive nature of histology analysis, an intensity-gradient based method [22] was applied to calculate cardiac myofiber orientation in histology images to facilitate the comparison between OPT and histology images. This method has been previously applied to imaging fiber orientation in OCT intensity images [7–9]. The two-dimensional gradient at each image pixel was first computed using a 3 × 3 Sobel edge detector. Then the magnitude and direction of the gradient at each pixel was obtained as:

$$G(i,j) = \sqrt{G_x^2(i,j) + G_y^2(i,j)}$$
$$\phi(i,j) = \tan^{-1}\frac{G_y(i,j)}{G_x(i,j)} \tag{1}$$

To improve signal-to-noise, the distribution of fiber orientation for all pixels within a sub-region (46 × 46 pixels) was assessed using the Von Mises distribution [22]. The most likely orientation corresponding to the peak of the Von Mises distribution was assigned to the center pixel within this region. The high resolution histology images had a pixel size of 0.25 μm/pixel. A window of 46 × 46 pixels was equivalent to 11.5 × 11.5 μm^2 which was the same as the OCT lateral resolution.

2.4 Surface refraction correction

The OPT and histology images were registered and compared as described below. First, the OPT image was transformed to correct the image distortion caused by surface refraction [23, 24]. This is an important step to improve the accuracy of the direct comparison between histology and OPT images. As described previously in ophthalmology imaging [23, 24], optical refraction at tissue surface deviates the incident beam, which distorts the planar image

#213714 - $15.00 USD Received 9 Jun 2014; revised 24 Jul 2014; accepted 24 Jul 2014; published 29 Jul 2014
(C) 2014 OSA

plane. In addition, the measured optical axis in JMOCT is within the imaging plane perpendicular to the light beam which may deviate from the original incident direction due to optical refraction at the same surface. As illustrated in Fig. 1, this plane is rotated away from the global *en face* B-C plane due to surface refraction and needs to be projected to the B-C plane (equivalent to the histology plane).

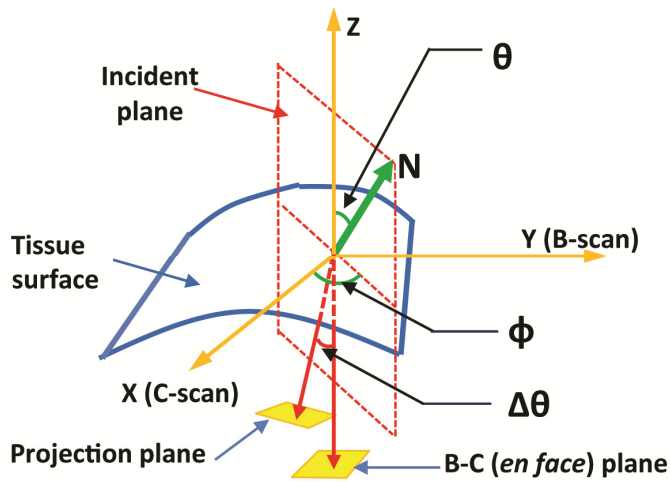

Fig. 1. An illustration of image distortion induced by surface refraction. The incident light (A-scan) is aligned with the z-axis. (**N**) is the surface normal vector at the light incidence point. The *en face* x-y plane formed by the B- and C-scan are equivalent to the histology sectioning plane. The incident light is deviated by Δθ within the incident plane (formed by the incident light and the surface normal vector) due to optical refraction at the sample surface.

To correct surface refraction, the sample surface in the OCT intensity image was first determined using an intensity threshold-based segmentation algorithm [12]. The resulting surface data were represented as a 2D array containing the axial depth position for each pixel on the sample surface. We applied a 5 × 5 median filter to remove noisy pixels from the data set. The surface normal vector **N** = $[N_x,N_y,N_z]$ was then calculated by using the "surfnorm" function in MATLAB.

As shown in Fig. 1, the surface normal vector $[N_x,N_y,N_z]$ can be described using a pair of angles (θ, ϕ):

$$\theta = \tan^{-1}\frac{\sqrt{N_x^2+N_y^2}}{N_z}. \qquad \phi = \tan^{-1}\frac{N_y}{N_x} \tag{2}$$

Due to surface refraction, the incident beam is deviated by an angle of Δθ within the incident plane which is formed by the incident light and the surface normal vector. Applying geometrical transformation, the actual pixel position (x', y', z') corresponding to the raw pixel (x, y, z) can be calculated as:

$$\begin{aligned} x' &= x + z\sin\Delta\theta\cos\phi \\ y' &= y + z\sin\Delta\theta\sin\phi, \\ z' &= z\cos\Delta\theta \end{aligned} \tag{3}$$

#213714 - $15.00 USD Received 9 Jun 2014; revised 24 Jul 2014; accepted 24 Jul 2014; published 29 Jul 2014
(C) 2014 OSA

where the surface refraction induced direction change Δθ can be determined according to the Snell's law at the tissue surface:

$$\Delta\theta = \theta - \sin^{-1}\left(\frac{\sin\theta}{n}\right). \tag{4}$$

A value of 1.38 was used as the tissue refractive index n in our calculation. The fiber orientation angle β' measured in the global *en face* B-C plane can then be calculated as:

$$\beta' = \tan^{-1}\left(\frac{\cos\Delta\theta\cos\varphi\sin\beta - \sin\varphi\cos\beta}{\cos\Delta\theta\sin\varphi\sin\beta + \cos\varphi\cos\beta}\right), \tag{5}$$

where β is the directly measured orientation angle. The above correction procedure was applied to all pixels in the 3D OPT data set.

2.5 Image registration

The orientation of each histology image had random variations during the process of sectioning and mounting of histology slides. Therefore all histology images need to be aligned with each other. We first registered all histology images based on their boundary profiles obtained using a low magnification 2 × objective lens. A Matlab program was developed using the function "imregister" to register all histology images. This intensity-based automatic registration uses an optimization algorithm to find the best transformation to register two input images. We used "rigid" transformation (translation and rotation) to register all 2 × histology images. The pixel-wise mean square error was used as the optimization metric and an optimizer with a gradient magnitude tolerance of 10^{-4} and 300 iterations was used as the converging condition.

In addition, all histology images were registered with OCT intensity images using the same algorithm. Before applying the registration, the histology images were rescaled to have the same pixel resolution as the OCT images. The obtained translation and rotation values (t_B, t_C, α) for each histology slice were stored, where t_B and t_C are translational distances (in pixel) along the B- and C-scan, respectively, and α is the rotation angle along the A-scan direction. In order to obtain accurate fiber orientation from histology images, a 40 × objective lens was used to image the histology samples so that individual fibers can be resolved. After the fiber orientation was calculated using the algorithm described in Sec. 2.3, the stored transformation (t_B, t_C, α) was applied to register the histology tractographic image with OPT image.

3. Results and discussion

Figure 2 shows an example of the heart tissue image obtained in this study using the JMOCT system. The 3D OCT image of this piece of heart tissue is shown in Fig. 2(a) with the A-, B-, and C-scan directions marked. Figures 2(b)-2(f) show examples of *en face* images (within the B-C plane) extracted at ~0.56 mm beneath the epicardium surface. The measured average local retardation (Fig. 2(c)) was $1.72 \times 10^{-2} \pm 9.8 \times 10^{-3}$ rad/pixel. The measured average diattenuation (Fig. 2(d)) was $5.5 \times 10^{-3} \pm 4.7 \times 10^{-3}$/pixel. As explained in Sec. 2.2, these "local" values represented the effective tissue polarization properties within the corresponding single image pixel and were similar to those reported previously [20]. No fibrous structure can be discerned in the OCT intensity image (Fig. 2(b)) due to insufficient spatial resolution to resolve the individual muscle fibers in the mouse heart. However, the optical axis can still be clearly measured as shown in the pseudocolor image in Fig. 2(e). The streamline plot of the optical axis data was used to construct the tractographic representation of the fiber orientation (Fig. 2(f)).

#213714 - $15.00 USD Received 9 Jun 2014; revised 24 Jul 2014; accepted 24 Jul 2014; published 29 Jul 2014
(C) 2014 OSA

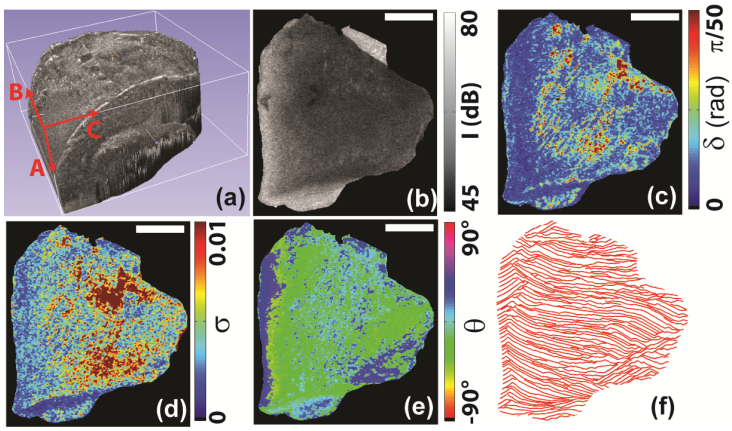

Fig. 2. (a) The 3D OCT intensity images obtained in a piece of heart tissue. The example *en face* images of (b) intensity (I), (c) local retardation (δ), (d) local diattenuation (σ), and (e) local optical axis (θ) extracted at a depth of 0.56 mm from surface. (f) A tractographic representation of fiber orientation using the streamline plot. The size bars in the images represent 0.5 mm.

3.1 Correcting surface refraction

The image distortion due to surface refraction can significantly impact the OPT accuracy. To illustrate this effect, Fig. 3(a) shows an example histology image obtained at a depth of 0.35 mm beneath the epicardium. Figure 3(b) shows the fiber orientation image obtained from the histology image as described in Sec. 2.3. Figures 3(c) and 3(d) show the OPT results before and after correcting the surface refraction.

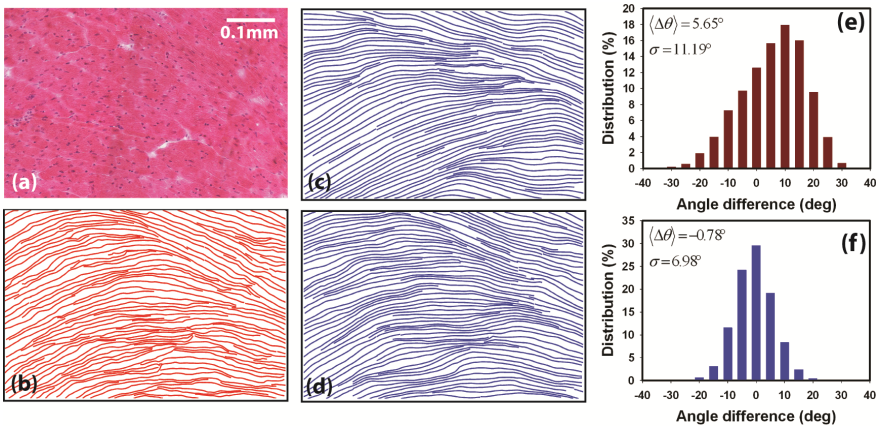

Fig. 3. An example of the surface refraction correction. (a) The histology image obtained at 0.35 mm beneath the epicardium surface. (b) The tractographic result obtained from the histology image. (c) The OPT result without correcting the surface refraction. (d) The OPT after surface refraction correction. The corresponding distribution of pixel-by-pixel difference between histology and OPT before and after correction are shown in (e) and (f), respectively.

Without correcting the surface refraction, the OPT results (Fig. 3(c)) were significantly different from the histology tractography (Fig. 3(b)). For example, the central part of the OPT shows positive orientations; whereas the orientation revealed in histology is close to zero degree. In addition, the fibers in the upper left corner of the histology result (Fig. 3(b)) show positive angles; whereas they remain almost horizontal in OPT (Fig. 3(c)). After applying the correction as describe in Sec. 2.4, the resulting OPT (Fig. 3(d)) appears very similar to the histology results (Fig. 3(b)). We noticed that most of the improvement was due to the position

#213714 - $15.00 USD Received 9 Jun 2014; revised 24 Jul 2014; accepted 24 Jul 2014; published 29 Jul 2014
(C) 2014 OSA

correction using Eq. (3). The orientation change (Eq. (5)) only induced minimal changes in the resulting orientation, likely due to the relative flat surface of the tissue samples.

To further quantify the differences between histology and OPT, the pixel-by-pixel differences between the two images were calculated. The histology images were resized using cubic spline to match the pixel size of 3.9 μm in OPT. As shown in Fig. 3(e) and 3(f), the mean difference between histology and OPT was reduced from 5.65° before correction to −0.78° after correction. The correction reduced standard deviation from 11.19° to 6.98°. After the distortion correction, about 85.5% of the 14,959 pixels in this image area (Fig. 3(a)) had a ≤ 10° difference in measured orientation between OPT and histology. Even though this pixel-wise comparison did not reach a perfect 100% match, the corrected OPT (Fig. 3(d)) and histology result (Fig. 3(b)) resembled each other remarkably well. As explained later in this section, tissue variations introduced during histology processing made it extremely challenging to obtain a perfect pixel-wise match.

3.2 Depth profile of fiber orientation

A major feature of the myofiber architecture in heart is the unique "cross-helical" pattern where the myocardial fibers rotate from negative angles at epicardium to positive angles at endocardium [25]. To verify OPT, we calculated the depth profile of fiber orientation in each animal tissue and compared the results with histology. A total of 21 small regions of interest (ROIs) with a size of 92 × 92 μm^2 each were evaluated with 3 ROIs selected from each mouse heart. The average value and standard deviation of fiber orientation were obtained using both histology and OPT images from the epicardium to 1-mm in depth. Because the high resolution histology images of these ROIs were acquired using a 40 × objective, they had a very limited field of view. To ensure a consistent ROI position in each histology image at different depths, their positions were carefully examined in relation to the tissue boundaries among adjacent histology slices and with the assistance of image registration as described in Sec. 2.5. As explained in Sec. 2.1, the histology slices had a thickness of 10 μm, whereas OPT had an axial pixel size of 3.9 μm. To facilitate the comparison, cubic spline interpolation was applied to resize the OPT axial pixel to the same size of 10 μm as in histology.

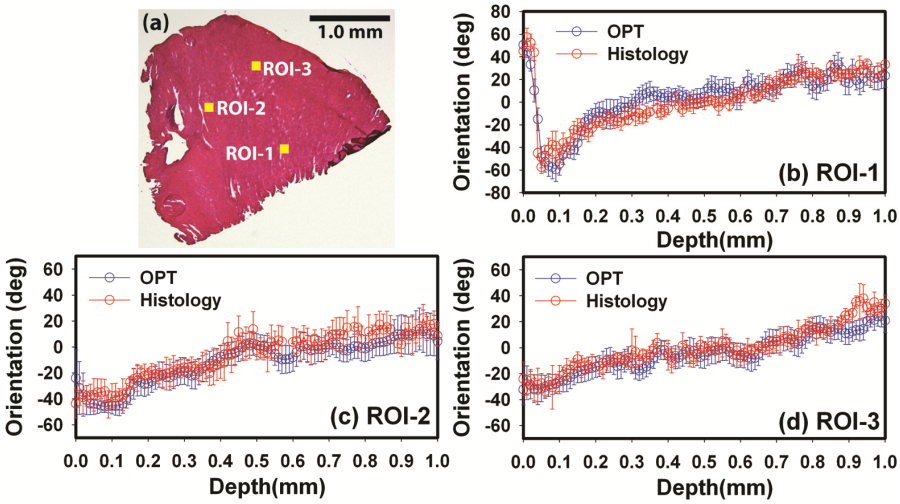

Fig. 4. A direct comparison of the depth-resolved myocardial fiber orientation measured from histology and OPT. The three ROIs were selected from the heart sample as shown in (a). The size of the ROI is 92 × 92 μm^2. Error bars indicate standard deviation.

Figure 4 shows an example depth profiles of fiber orientation obtained from 3 ROIs in a piece of heart sample. This tissue sample was excised from the left ventricle of the mouse

#213714 - $15.00 USD Received 9 Jun 2014; revised 24 Jul 2014; accepted 24 Jul 2014; published 29 Jul 2014
(C) 2014 OSA

heart. There were a few data points missing in the histology results due to damaged tissue slices during sectioning. The fiber orientation in ROI-2 and 3 had similar depth profiles with fibers oriented at −30° to −50° at epicardium and transiting to + 20° to + 40° at 1.0 mm depth following an approximately linear trend. At the location of ROI-1, however, the orientation of myocardial fibers showed a different depth profile. The fibers had a positive orientation at epicardium and rotated clockwise to negative angles at ~50 μm. The fibers then reversed the trend and started to rotate counterclockwise and eventually reached to ~-20° at 1 mm beneath the epicardium. Despite the differences, all three curves revealed the typical global cross-helical structure in cardiac muscle, i.e. a transition from negative fiber orientation close to epicardium to positive fiber orientation toward endocardium. These curves transitioned from negative angles to positive angles at ~0.5 mm.

Overall, the OPT and histology results agreed very well in these three ROIs. In addition, the standard deviation obtained in each ROI was comparable in both histology and OPT results. Quantitatively the OPT and histology results were highly correlated with each other. The obtained coefficients of determination were R^2 = 0.88, 0.94, 0.90 for ROI-1, 2, and 3, respectively. As discussed in our previous study [20], the reversed trend in ROI-1 observed within the first 50 μm beneath the epicardium was not previously reported in the diffusion tensor MRI (DTI) images of mouse heart, most likely due to the insufficient spatial resolution in DTI. Nevertheless this observation has been clearly validated in histology images (Fig. 4(b)).

Figure 5(a) shows the overall correlation (R^2 = 0.85) of the OPT and histology results obtained in all seven mice. The entire data set had over 2,000 data points obtained from a total of 21 depth profiles from 0 to 1.0 mm depth with a step size of 10 μm. Figure 5(b) shows the distribution of the difference in orientation angles calculated using these two methods. The obtained histogram can be well fitted using a Gaussian function (adj-R^2 = 0.994) $a \times \exp\left[-\left(x-x_0\right)^2/\left(2\sigma^2\right)\right]$. The fitted mean difference is $x_0 = 1.0°$ with a standard deviation of σ = 9.1°. A total 82.2% of the data points had a difference ≤ 10°. Such a level of consistence between OPT and histology exceeded the correlation between histology and diffuse tensor based MRI reported in a previous study [26].

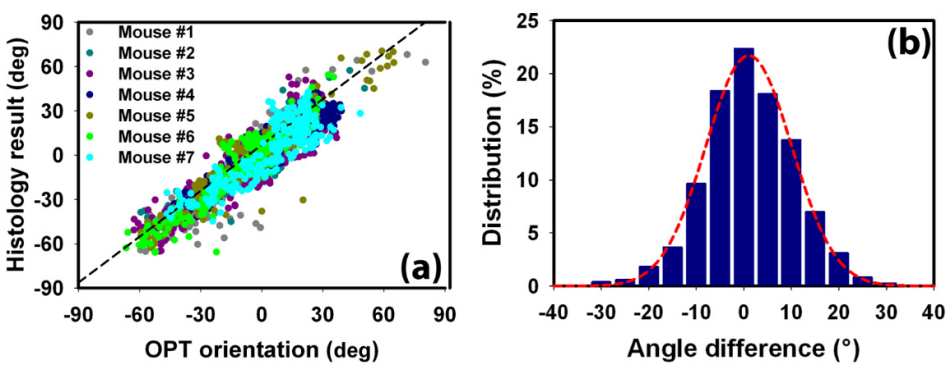

Fig. 5. (a) The linear correlation between OPT and histology results (R^2 = 0.85). (b) The distribution of the difference between the fiber orientation angles measured using OPT and histology. The data represented depth-resolved orientation (Fig. 4) measured from a total of 21 ROIs selected from the heart samples in 7 mice. The red dashed line in (b) represents a Gaussian fitting.

3.3 Pixel-wise comparison between OPT and histology

In order to better understand the differences between OPT and histology measurements, we investigated the pixel-wise differences between the two tractographic images. The high

#213714 - $15.00 USD Received 9 Jun 2014; revised 24 Jul 2014; accepted 24 Jul 2014; published 29 Jul 2014
(C) 2014 OSA

resolution histology images acquired using a 40 × objective had a limited field of view of 256 × 320 μm^2. To obtain the histology image of a large histology slice, multiple overlapping histology images of the same slice were acquired and then manually stitched together using the Photoshop software. Because this manual stitching process is time consuming, we constructed the large histology images at two depths of ~0.35 mm and ~0.65 mm in each tissue sample. To register these large histology images with OPT images, the image registration described in Sec. 2.5 was fine-tuned by transforming the histology images within a 50 μm translational range and 5° rotational range around the original transformation parameters (t_B, t_C, α) obtained using sample boundary profiles. The final registration transformation was selected if it produced the minimal root-mean-square (RMS) value of the pixel-by-pixel difference between the histology and OPT. The resulting adjustments in the 14 images (2 evaluation depths in each of the 7 samples) were between –27.3 μm to + 35.1 μm in translation and –2.2° to + 1.3° in rotation. These small adjustment values suggested the good accuracy in the original image registration.

Figure 6 shows an example comparison between the histology tractography and OPT obtained in a tissue sample excised from the right ventricle of a mouse heart. The tractography was overlaid over corresponding histology and OCT intensity images. The size of the image is 1.0 × 1.0 mm^2. The histology images were resized to have the same pixel size of 3.9 μm as the OPT images. The muscle fibers at 0.34 mm beneath the epicardium showed a trapezoid type organization, i.e. the fibers entered at the left side with positive angles, transited into horizontal orientation at the middle, and then left the area with negative angles from the right side. In comparison, the fiber organization at 0.66 mm beneath the epicardium appeared more homogeneous with all fibers crossing the entire area with positive orientations.

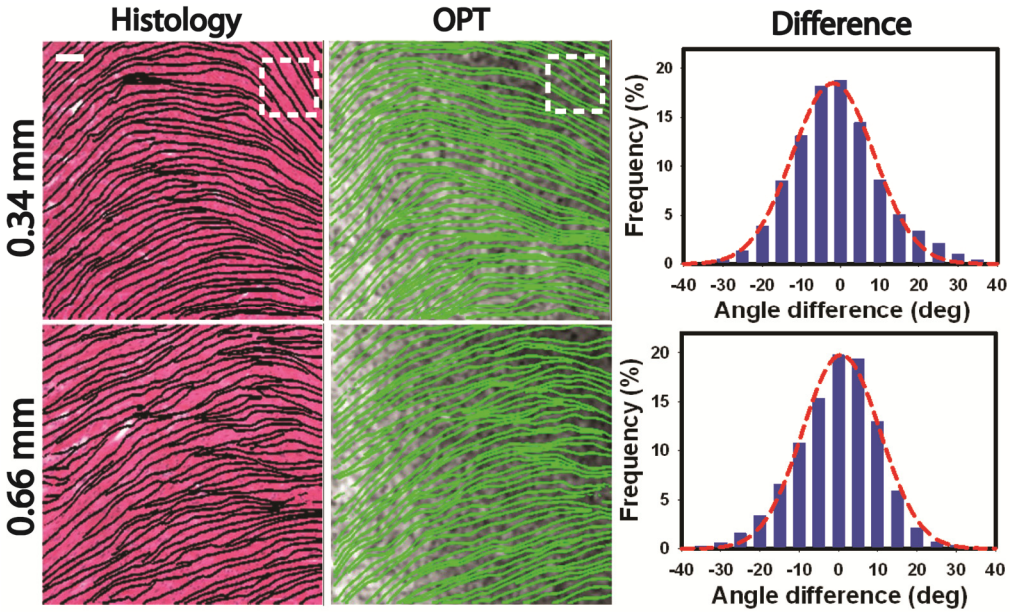

Fig. 6. An example comparison of tractography computed using OPT and histology at depths of 0.34 mm and 0.66 mm from the epicardium in a heart tissue sample. The corresponding tractography was overlaid over the histology and OCT intensity images, respectively. Also shown are the corresponding distributions of the pixel-by-pixel orientation difference, in which the dashed lines were fitting results using a Gaussian function. The white dashed boxes highlight the difference between histology and OPT. The size bar indicates 100 μm.

Overall, very similar fiber orientation patterns were revealed in both histology and OPT results. The distributions of the pixel-by-pixel difference were calculated for a quantitative comparison. As shown in Fig. 6, both distributions fitted well (R^2>0.99) using a Gaussian

#213714 - $15.00 USD Received 9 Jun 2014; revised 24 Jul 2014; accepted 24 Jul 2014; published 29 Jul 2014
(C) 2014 OSA

function. The fitting mean difference and standard deviation are $x_0 = -1.9°$, b = 10.4° for 0.34 mm depth and $x_0 = -0.7°$, b = 9.9° for 0.66 mm depth. At the 0.34 mm depth, 63.5% of the 65,536 pixels had ≤10° difference between OPT and histology; whereas the percentage was slightly higher at 67.9% for the results obtained at the depth of 0.66 mm. If the difference threshold was set as 15°, the percentage became 80.9% and 85.7% for 0.34 mm and 0.66 mm, respectively. Among all 14 large scale comparisons, the percentage of pixels with ≤15° difference between OPT and histology ranged from 69.9% to 95.5%.

3.4 Error analysis

Each of these large images was visually examined in detail to understand the difference between histology and OPT at pixel level. For the sample shown in Fig. 6, despite the overall good agreement between OPT and histology, there is a difference at the upper right corner (marked with dashed lines) of the tractography obtained at 0.34 mm. Specifically, the fibers in OPT within the box in Fig. 6 were more inclined toward the horizontal direction. A close analysis revealed that this difference was due to imperfect alignment between the *en face* OPT and histology slices. Although the histology processing was prepared by an experienced staff and under great care, the histology-sectioning plane may be slightly different from the *en face* plane (Fig. 7(a)). Indeed, as shown in Figs. 7(a)-7(d), the difference in the aforementioned upper-right corner in Fig. 6 was significantly reduced after moving the slice position 35 μm toward the epicardium (tilting the *en face* plane for ~2° along the diagonal line in Fig. 6).

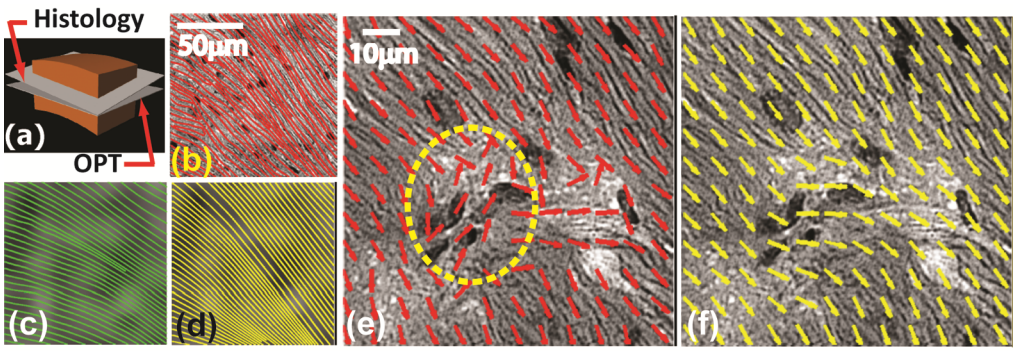

Fig. 7. (a) The potential misalignment between the histology sectioning plane and *en face* OCT scanning plane. (b) The histology tractography and (c) OPT in a tissue sample located at 0.34 mm beneath the epicardium. (d) OPT results of the same tissue region with the *en face* plane tilted 2.0°. (e) The high resolution histology tractography and (f) OPT in a tissue region with intensity variations.

In addition, we found that many of the differences between OPT and histology tractography can be attributed to those incorrect fiber orientations obtained in histology analysis. The edge detection used to identify fiber structures was also affected by any intensity changes that are not related to muscle fibers. For example, vessels, scars or tissue damage from histology processing all appeared with different pixel intensities in histology images. As an example, Fig. 7(e) shows a tissue section with a cluster of nuclei and light-colored tissue components at the center (circled with a dashed line). To facilitate the comparison, both tractographic results were visualized using quiver plot and overlaid on the histology image. Evidently, these fiber irrelevant spatial intensity variations produced incorrect fiber orientation data in the high resolution histology tractography. On the other hand, optical axis measurement is independent of such intensity variations in the sample. As a result, the OPT result appeared to follow the fiber tracts correctly (Fig. 7(f)). Unfortunately such incorrect histology fiber tracking contributed to the difference between histology tractography and OPT.

#213714 - $15.00 USD Received 9 Jun 2014; revised 24 Jul 2014; accepted 24 Jul 2014; published 29 Jul 2014
(C) 2014 OSA

Finally, it is known that the geometric shape of the tissue and its fiber organization may be altered during the histology processing. The histology sectioning process may cause tissue deformation and even tearing. At the proxy of these alterations, the tissue morphology was changed. Although these changes may not significantly impact the overall fiber organization, they greatly affected the pixel-wise comparison. We observed that large pixel-by-pixel differences between OPT and histology may appear at location with significant changes in fiber organization, e.g. fiber transition, splitting and merging. At such locations, any small morphological alteration may induce a large pixel-wise difference due to the high spatial resolution. Figure 8 shows an example comparison of a 1.0 × 1.0 mm^2 tissue from the left ventricle of a mouse heart. This pair of images had the largest overall pixel-by-pixel difference among all samples we examined. Only 69.9% of the pixels in the image had a difference ≤15° between histology and OPT. Still, the OPT reliably reproduced all key features of fiber organization in the piece of sample as shown in Fig. 8. The fiber transitions marked by dashed circles (#1 and #2) at the left and right sides of the images were very similar in both images. Tissue tearing appeared in the middle part of the histology image (Fig. 8(a)), which was coincident with the location showing the largest differences between the two tractography results. Such tissue tearing induced morphological changes in the surrounding region. As a consequence, the fiber organization in the middle region (circle #3) appeared similar but the exact shape and position were changed. Such image deformation at microscopic scales may be more accurately handled using more sophisticated image registration algorithms [27]. Nevertheless, OPT and histology results remained consistent in regions not affected by such histology artifacts.

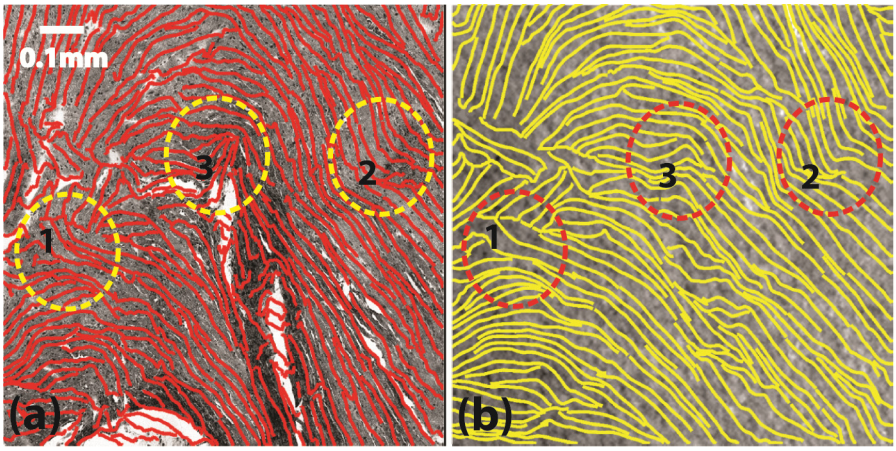

Fig. 8. A comparison of the (a) histology tractography and (b) OPT in a tissue sample with a significant amount of orientation changes and tissue deformation caused by histology processing. The corresponding tractography results were overlaid over the histology and OCT intensity images, respectively.

4. Conclusions

In this study, we compared depth-resolved fiber orientation mapping in fresh heart samples obtained by using OPT and histology images. We developed a systematic set of image processing methods to correct image distortions in OPT induced by surface optical refraction and to register OPT with histology images. The results indicated that OPT can reliably map the cardiac myofiber organization in fresh mouse heart. The fiber orientation measured in OPT agreed very well with histology results. A detailed pixel-wise analysis indicated that the majority of the differences between OPT and histology can be attributed to imperfect alignment between histology and OPT, tissue alterations during histology processing, as well as artifacts when extracting fiber orientation in histology images. In addition, deteriorating

#213714 - $15.00 USD Received 9 Jun 2014; revised 24 Jul 2014; accepted 24 Jul 2014; published 29 Jul 2014
(C) 2014 OSA

signal to noise at larger depths eventually led to inaccurate fiber orientation calculation. As a result, the image depth of our current system was limited to 1.0 mm in fresh heart tissue. Nevertheless, the OPT technology opens a new way for imaging the important cardiac myofiber architecture in fresh heart samples. With its combined advantages of fast speed, large field of view and high resolution, OPT is especially attractive for imaging applications in small animal models. If implemented in a fiber optics based PSOCT system, this technology may be integrated into catheter based system for *in vivo* endoscopic imaging.

Acknowledgments

Author D. Duan acknowledges support from NIH HL-91883 and Parent Project Muscular Dystrophy.